Available online at www.sciencedirect.com
SCIENCE DIRECT®
Journal of Sound and Vibration 280 (2005) 611–631
JOURNAL OF SOUND AND VIBRATION
www.elsevier.com/locate/jsvi

Dynamic stability of liquid-filled projectiles under a thrust

S.-W. Jung, K.-S. Na, J.-H. Kim*

School of Mechanical and Aerospace Engineering, Seoul National University, San 56-1, Shinrim-Dong, Kwanak-Ku, Seoul 151-742, South Korea

Received 1 July 2003; accepted 12 December 2003

Abstract

Fluid–structure interaction (FSI) problem is investigated to study the dynamic stability of liquid-filled projectiles under a thrust. The projectile is modelled as a flexible cylindrical shell, and the thrust is modelled by the constant and pulsating follower force. To analyze the fluid and structure simultaneously, hydrodynamic pressure of the liquid and elastic deformation of the structure are taken into consideration. We assume that the fluid is incompressible and having free-surface effect. In the numerical study, natural frequencies for various filling ratios of liquid of the cylindrical shells are analyzed and compared with the previous experimental and theoretical works for with and without the free-surface effect. Further, the results on dynamic stability of partially liquid-filled slender cylindrical shells under constant and pulsating follower force for various filling ratios of the fluid are summarized. Lastly, the effects of length and thickness of the shell are studied in detail.

1. Introduction

Fluid–structure interaction (FSI) problems have attracted great attention from engineers due to its wide practical applicability such as in the design of launch vehicles, marine platforms, nuclear power plants, etc.

Generally, the dynamic characteristics of an elastic body are different from a body containing a fluid medium. That is to say, when an elastic structure vibrates, the hydrodynamic pressure is developed. Further, the pressure modifies the deformation of the structure, which, in turn, affects the hydrodynamic pressure. Therefore, the structure and the fluid should be considered as a single coupled system.

*Corresponding author. Tel.: +82-2880-7383; fax: +82-2887-2662.
E-mail address: jwhkim@snu.ac.kr (J.-H. Kim).

0022-460X/$ - see front matter © 2004 Elsevier Ltd. All rights reserved.
doi:10.1016/j.jsv.2003.12.016

In the analysis of liquid-storage tanks, the formulation of the hydrodynamic pressure field has been a major research topic as shown in Ref. [1]. Some of the studies conducted in connection to this subject are as follows. Housner [2] assumed liquid as an ideal flow, but neglected the container flexibility and the free surface of the liquid. Veletsos and Yang [3] emphasized the importance of the flexibility of the container in the dynamic modelling of liquid motion. Morand and Ohayon [1,4,5] proposed general numerical formulations for coupled systems.

FSI can be classified into three categories, such as sloshing, hydroelastic, and vibroacoustic modes [4–7]. Among them, liquid propellant rocket tend to experience dominant hydroelastic vibration, which is similar to the vibration of an elastic tank with incompressible and inviscid liquid without gravity effect. Particularly, hydroelastic longitudinal oscillations are involved in the so-called ''Pogo instability''. In actual cases, we would face with the simultaneous vibration of fluids and structures under gravity fields and prescribed excitation forces. At the same time, gravity can be viewed as a restoring force acting on the free surface. For sufficiently high frequency range, this force is negligible compared with the liquid dynamic forces. Thus, the frequencies of interest should be sufficiently above the sloshing natural frequency of the liquid, which can be computed for the same fluid domains and fixed fluid–structure contact surfaces [5].

Based on the finite element method, two basic approaches were used for the FSI problems. In the first approach, the fluid was characterized as a single pressure or velocity potential variable at each node of the finite element mesh [6–8], and then the fluid and structure were coupled through the fluid–structure interface. The coupled set of equations is, in general, unsymmetric. In the second approach, the displacement formulation [9,10] was such that the fluid motion is expressed in terms of the nodal displacements. By doing so, compatibility and equilibrium along the interface are automatically satisfied. The fluid is modelled as elastic solid with negligible shear modulus. This assumption of negligible shear modulus leads to the appearance of non-physical ''circulation'' modes. Different techniques have been introduced to eliminate these non-physical modes [11,12]. The main advantage of this approach is its similarity between the discretized forms of the fluid and the structure. Another way to describe the fluid motion is to use both the displacement or velocity potential and the acoustic pressure altogether [1,5,13]. Then, the resulting finite element equations would become symmetric, and the circulation modes could be avoided without having to use penalty terms to restore the inviscid nature of the fluid. In this study, we adopt this so-called mixed formulation.

Especially, space shuttle and intercontinental ballistic missile have been using liquid propellant rocket to produce a large thrust within a short time interval. For this reason, a propellant tank is built in large size, and the liquid–structure interaction in a fuel tank has been an important issue.

In this paper, we modelled a thrust as a constant and pulsating follower force [14], and FSI is considered for investigating the dynamic stability of partially liquid-filled cylindrical shells. A variational principle for FSI including the compressibility of the fluid is considered as in Refs. [5,7]. Then, a mixed formulation is used to generate a symmetric coupled set of equations for incompressible and inviscid fluid. To check the validity of the finite element method in this study, we compare the natural frequencies of partially filled clamped-free water tanks with and without free-surface effect with previous works. In addition, we considered the hydroelastic vibration of a structure under a thrust for various lengths, thicknesses, and filling ratios to analyze the structure's dynamic stability.

2. Formulation

2.1. Fluids and structures

Vibration of the launcher is accompanied by fluctuations in the liquid pressures, especially at the fuel feed inlets in the propulsion unit, which induces pressure and feed rate oscillations, and consequently, fluctuations in the rocket engine thrust, together with oscillatory forces at the anchor points of structure lines of the launcher. These forces can develop to increase the launcher vibrations, and hence lead to an instability known as the "Pogo" effect. This study focuses on the fluid–structure interaction by using the simplified model for partially-filled cylindrical shells under a thrust as shown in Fig. 1. In this, finite element meshes consist of cylindrical shell elements, fluid solid elements, and interface elements. To obtain a symmetric finite element formulation, we describe the fluid by pressure (P) and displacement potential (φ), respectively.

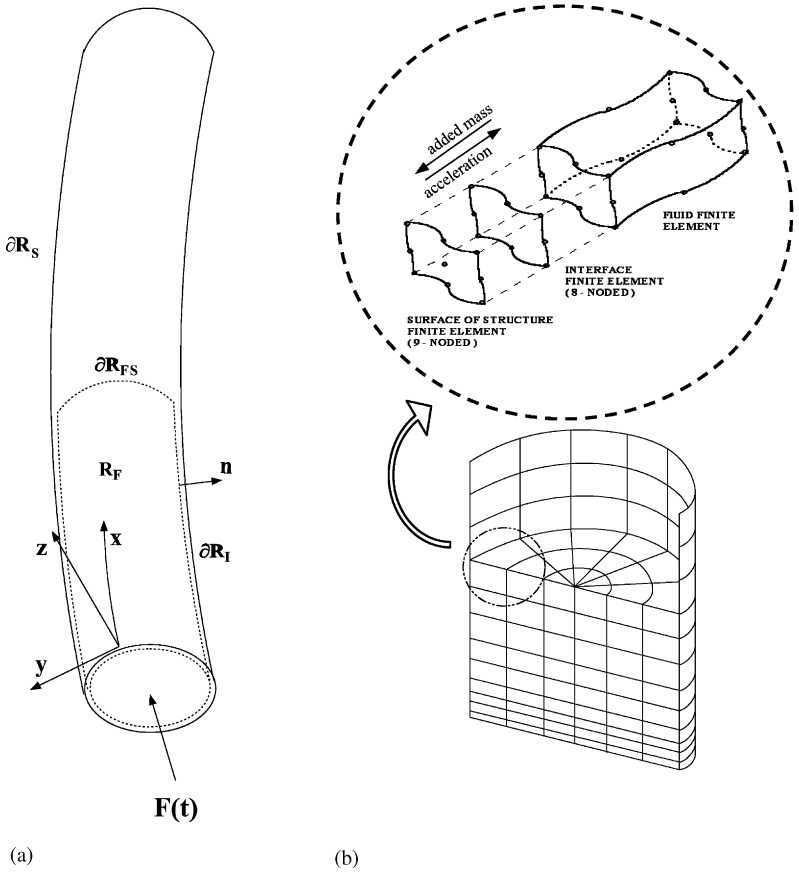

Fig. 1. Simplified model of launcher and finite element mesh.

2.1.1. Fluids

The motion of an isothermal, inviscid fluid with small disturbance is governed by

$$\textit{Continuity equation}: \dot{\rho}_F + \rho_F v_{i,i} = 0 \quad \text{in } R_F, \tag{1}$$

$$\textit{Euler equation}: \rho_F \dot{v}_i = \tau_{ij,j} \quad \text{in } R_F, \tag{2}$$

$$\textit{Barotropic equation}: \dot{P} = \frac{B}{\rho_F}\dot{\rho}_F = 0 \quad \text{in } R_F, \tag{3}$$

where ρ_F is the fluid density, v_i is the velocity component, and τ_{ij} is the Cauchy stress tensor given by

$$\tau_{ij} = -P\delta_{ij},$$

where P is the pressure, δ_{ij} is the Kronecker Delta and B is the bulk modulus. Throughout this paper, a standard indicial notation is used; subscripts denote the components of tensors and repeated subscripts imply a sum of all the index. In addition, a comma followed by a subscript denotes a partial derivative with respect to the corresponding spatial variable, whereas a superimposed dot denotes the time derivative. The continuity equation (1) can be combined with Eq. (3) of state to yield

$$\frac{1}{B}\dot{P} + v_{k,k} = 0 \quad \text{in } R_F. \tag{4}$$

Similarly, the Euler equation (2) can also be combined with the constitutive equation to yield

$$\rho \dot{v}_i = -P_{,i} \quad \text{in } R_F. \tag{5}$$

To formulate the fluid–structure interaction problem, the fluid boundary ∂R_F is divided into two parts, such as the free-surface boundary ∂R_{FS}, the fluid–structure interaction boundary ∂R_I, and the prescribed traction boundary. The latter boundary is set to zero in this formulation. The unit outward normal to ∂R_F is denoted by n_i. To eliminate the rotational part of the velocity field, a displacement potential, φ, is introduced such that

$$v_i = \dot{\varphi}_{,i} \quad \text{or} \quad u_i^F = \varphi_{,i} \quad \text{in } R_F \tag{6}$$

and $u_{,i}^F$ is the fluid displacement.

With this definition, the free-surface displacement u_g^F is related to P by

$$P = \rho_F g u_g^F \quad \text{or} \quad u_g^F = \varphi_{,i} n_i = \frac{1}{\rho_F g} P \quad \text{on } \partial R_{FS}. \tag{7}$$

Substituting Eq. (6) into Eqs. (4) and (5), respectively, then the continuity equation becomes

$$\frac{1}{B}P + \varphi_{,ii} = 0 \quad \text{in } R_F \tag{8}$$

and the momentum equation can be obtained as

$$P + \rho_F \ddot{\varphi} = 0 \quad \text{in } R_F. \tag{9}$$

Eqs. (7)–(9) can be derived by considering the variation of the functional with Lagrange multipliers given by

$$\delta\pi_f = \delta\left[\int_{t_0}^{t_1}\int_{R_F}\left(\tfrac{1}{2}\rho_F\dot{\varphi}_{,i}\dot{\varphi}_{,i} - \frac{1}{2B}P^2\right)\mathrm{d}R_F\,\mathrm{d}t + \int_{t_0}^{t_1}\int_{\partial R_{FS}}\left(-\frac{1}{2\rho_F g}P^2\right)\mathrm{d}\partial R_{FS}\,\mathrm{d}t + \int_{t_0}^{t_1}\int_{R_F}\lambda_1(P+\rho_F\ddot{\varphi})\,\mathrm{d}R_F\,\mathrm{d}t + \int_{t_0}^{t_1}\int_{\partial R_{FS}}\lambda_3(P+\rho_F\ddot{\varphi})\,\mathrm{d}\partial R_{FS}\,\mathrm{d}t\right] = 0, \tag{10}$$

where the first integral involves the kinetic and potential energies, the second term is the free-surface potential energy, and λ_1, and λ_3 are the Lagrange multipliers that have to be determined.

To include fluid–structure interaction, $\delta\pi_F$ is redefined as

$$\delta\pi_F = \delta\pi_f + \delta\left[\int_{t_0}^{t_1}\int_{\partial R_I}(-Pu_i n_i)\,\mathrm{d}\partial R_I\,\mathrm{d}t + \int_{t_0}^{t_1}\int_{\partial R_I}\lambda_2(P+\rho_F\ddot{\varphi})\,\mathrm{d}\partial R_I\,\mathrm{d}t\right], \tag{11}$$

where the first additional term is the work done due to the structural displacement u_i around ∂R_I, and the second term enforces the equilibrium between P and φ with λ_2 as a Lagrange multiplier.

2.1.2. Structures

An assumed independent strain formulation is applied to derive the eighteen-node solid element for shell analysis [15,16]. Hamilton's principle is applied to a shell subjected to a constant and pulsating follower force as follows:

$$\delta\pi_S = \delta\int_{R_s}\tfrac{1}{2}\rho_s\dot{u}_i\dot{u}_i\,\mathrm{d}R_S + \delta\int_{R_s}\tfrac{1}{2}\tau_{ij}\varepsilon_{ij}\,\mathrm{d}R_S + \delta W_f, \tag{12}$$

where the first and second terms represent the kinetic energy and the strain energy, respectively. In addition, δW_f is the virtual work of the follower force. In addition, the axial stress is linearly distributed along the longitudinal direction [17], and that the axial stress is uniformly distributed in the thickness direction [18], then δW_f can be expressed as

$$\delta W_f = \int_0^{2\pi}\int_0^L \frac{F(t)}{L}(L-x)\left(\frac{\partial\delta w}{\partial x}\frac{\partial w}{\partial x} + \frac{\partial\delta v}{\partial x}\frac{\partial v}{\partial x}\right)R\,\mathrm{d}x\,\mathrm{d}\theta + \int_0^{2\pi}F(t)\left(\delta w\frac{\partial w}{\partial x} + \delta v\frac{\partial v}{\partial x}\right)R\,\mathrm{d}\theta\Big|_{x=0}, \tag{13}$$

In the present analysis, the dynamic stability is examined for two special cases of $F(t)$. First, $F(t)$ has a constant magnitude as

$$F(t) = F_0. \tag{14}$$

Second, $F(t)$ has a harmonically pulsating part as well as a constant part as

$$F(t) = F_0 + F_1\cos(\omega_f t). \tag{15}$$

The dynamic instabilities of the two cases are very different from each other in the aspect of the method of analysis and the physical meaning.

2.1.3. A three-field mixed variational formulation

FSI problem can be obtained by combining the functionals for the structure and the fluid, such as Eqs. (11) and (12), respectively:

$$\delta\pi = \delta\pi_S + \delta\pi_F. \tag{16}$$

The variational formulation for compressible, irrotational, and inviscid fluid and the structure is given by [5,7]

$$\begin{aligned}\delta\pi = {} & \delta\int_{R_S} \tfrac{1}{2}\rho_S \dot{u}_i\dot{u}_i \,\mathrm{d}R_S + \delta\int_{R_S} \tfrac{1}{2}\tau_{ij}\varepsilon_{ij}\,\mathrm{d}R_S + \delta W_f \\ & + \delta\int_{R_F}\left(\tfrac{1}{2}\rho_F\dot{\varphi}_{,i}\dot{\varphi}_{,i} + \frac{1}{2B}P^2 + \frac{\rho_F}{B}P\ddot{\varphi}\right)\mathrm{d}R_F + \delta\int_{\partial R_I}(\rho_F u_i n_i \ddot{\varphi})\,\mathrm{d}\partial R_I \\ & + \delta\int_{\partial R_{FS}}\left(\frac{P^2}{2\rho_F g} + \frac{1}{g}P\ddot{\varphi}\right)\mathrm{d}\partial R_{FS}.\end{aligned} \tag{17}$$

2.2. Finite element equations

Finite element approximation of u_i, P, and φ are as follows:

$$u_i = N_j u_{ij}, \qquad P = S_j P_j, \qquad \varphi = H_j\varphi_j, \tag{18}$$

where N_j, S_j and H_j are the shape functions; u_{ij}, P_j and φ_j are the nodal structural displacement, displacement pressure and potential, respectively. Additionally, j is summed over the appropriate range of indices.

Matrices corresponding to the Eq. (17) are expressed symbolically as follows:

$$\int_{R_S}\delta\varepsilon_{ij}\tau_{ij}\,\mathrm{d}R_S + \delta W_f = \delta U^{\mathrm{T}}K_S U, \qquad \int_{R_S}\delta w_i\ddot{w}_i\,\mathrm{d}R_S = \delta U^{\mathrm{T}}M_S U, \tag{19a, b}$$

$$\int_{R_F}\rho_F\delta\varphi_{,i}\ddot{\varphi}_{,i}\,\mathrm{d}R_F = \delta\Phi^{\mathrm{T}}M_F\Phi, \qquad \int_{R_F}\frac{\rho_F}{B}\delta p\ddot{\varphi}\,\mathrm{d}R_F = \delta P^{\mathrm{T}}M_{PF}\Phi, \tag{19c, d}$$

$$\int_{\partial R_{FS}}\frac{1}{\rho_F g}\delta pp\,\mathrm{d}\partial R_{FS} = \delta P^{\mathrm{T}}K_P^{FS}P, \qquad \int_{R_F}\frac{1}{B}\delta pp\,\mathrm{d}R_F = \delta P^{\mathrm{T}}K_P P, \tag{19e, f}$$

$$\int_{\partial R_I}\delta w_i n_i\rho_F\ddot{\varphi}\,\mathrm{d}\partial R_I = \delta U^{\mathrm{T}}M_{SF}\Phi, \qquad \int_{\partial R_{FS}}\frac{1}{g}\delta p\ddot{\varphi}\,\mathrm{d}\partial R_{FS} = \delta P^{\mathrm{T}}M_{PF}^{FS}\Phi. \tag{19g, h}$$

Then the set of three matrix equations is obtained as

$$\begin{aligned} M_S\ddot{u} + K_S u + M_{SF}\ddot{\varphi} &= 0, \\ K_P P + M_{PF}\ddot{\varphi} + K_P^{FS}P + M_{PF}^{FS}\ddot{\varphi} &= 0, \\ -M_F\ddot{\varphi} + M_{PF}^{\mathrm{T}}\ddot{P} + M_{SF}^{\mathrm{T}}\ddot{u} + (M_{PF}^{FS})^{\mathrm{T}}\ddot{P} &= 0. \end{aligned} \tag{20}$$

Rearranging terms in the above equations, the equation of motion for the system can be written as [1],

$$\tilde{M}\ddot{q} + \tilde{K}q = 0, \tag{21}$$

where the generalized mass matrix and stiffness matrix are symmetric and are given by

$$\tilde{M} = \begin{bmatrix} M_S + M_{SF}M_F^{-1}M_{SF}^{\mathrm{T}} & M_{SF}M_F^{-1}(M_{PF} + M_{PF}^{FS})^{\mathrm{T}} \\ sym. & (M_{PF} + M_{PF}^{FS})M_F^{-1}(M_{PF} + M_{PF}^{FS})^{\mathrm{T}} \end{bmatrix}$$

and

$$\tilde{K} = \begin{bmatrix} K_S & 0 \\ 0 & (K_P + K_P^{FS}) \end{bmatrix}.$$

For an incompressible fluid, Eq. (17) can be simplified as bulk modulus (B) approaches infinity so that the governing equation of motion for an incompressible FSI problem with free surface is given by

$$M^*\ddot{q}^* + K^*q^* = 0, \tag{22}$$

where

$$M^* = \begin{bmatrix} M_S + M_{SF}M_F^{-1}M_{SF}^{\mathrm{T}} & M_{SF}M_F^{-1}(M_{PF}^{FS})^{\mathrm{T}} \\ sym. & (M_{PF}^{FS})M_F^{-1}(M_{PF}^{FS})^{\mathrm{T}} \end{bmatrix}$$

and

$$K^* = \begin{bmatrix} K_S & 0 \\ 0 & K_P^{FS} \end{bmatrix}.$$

Now we will consider the vibration of an elastic structure containing an incompressible liquid without free surface. The governing equation of hydroelastic vibration under a follower force is given by

$$([M_S] + [M_{SF}][M_F^{-1}][M_{SF}^{\mathrm{T}}])\{\ddot{u}\} + ([K_S] - F(t)[K_F])\{u\} = 0, \tag{23}$$

where u is a vector consisting of u_i, v_i and w_i and K_F is the stiffness matrix due to the follower force. Eigenvalues of these equations are the natural frequencies of fluid–structure interaction system, and we assume that 6 rigid-body modes (translation with respect to x, y or z directions, spinning with respect to x, y or z direction) can be controlled by the proper control equipment.

2.2.1. Constant follower force

By introducing non-dimensional parameters such as $x/R, z/R, L/R$, and t/R, we can obtain the following parameters [18]:

$$\beta(t) = F(t)\frac{(1-\nu^2)}{Et}, \tag{24}$$

$$\lambda^2 = \omega^2\frac{(1-\nu^2)\rho_S R^2}{E}, \tag{25}$$

$$\tau = t\left(\frac{E}{(1-\nu^2)}\rho_S R^2\right)^{1/2}. \tag{26}$$

Using these parameters and Eq. (14), Eq. (23) can be rewritten as

$$[\bar{M}]\{\ddot{\bar{u}}\} + ([\bar{K}_e] - \beta_0[\bar{K}_f])\{\bar{u}\} = 0, \tag{27}$$

where $\beta_0 = F_0(1-\nu^2)/Et$ and $\bar{M}$, $\bar{K}_e$ and $\bar{K}_f$ are non-dimensional matrices. We can use these equations to analyze the dynamic stability of the liquid-filled cylindrical shell under a constant follower force. The stability of the cylindrical shell can be examined by checking the sign and the imaginary part of λ^2. The coalescence of two eigenvalues of Eq. (27) indicates a flutter-type instability, and the eigenvalues become complex numbers. If an eigenvalue of Eq. (27) reduces to zero, a divergence type instability occurs.

2.2.2. *Pulsating follower force*

In the case of a pulsating follower force, Eqs. (15) and (23) can be regarded as a system of Mathieu-Hill equations, and equation of this type can be analyzed by various methods. Nayfeh and Mook [19] introduced the method of multiple scales as follows.

Using Eq. (15) and Eqs. (24)–(26), Eq. (23) can be written as

$$[\bar{M}]\{\ddot{\bar{u}}\} + [\bar{K}]\{\bar{u}\} + \varepsilon_1\beta_{cr}\cos(\lambda_f\tau)[\bar{K}_f]\{\bar{u}\} = 0, \tag{28}$$

where $[\bar{K}] = [\bar{K}_e] - \varepsilon_0\beta_{cr}[\bar{K}_f]$, $\varepsilon_0 = \beta_0/\beta_{cr}$, and $\varepsilon_1 = \beta_1/\beta_{cr}$. In addition, β_{cr} is the magnitude of β_0 at which a divergence or a flutter takes place for the case of a constant follower force.

We take only the constant part of the follower force into account in Eq. (23). In such case, the eigenvalue problem is obtained as mentioned in the preceding paragraph. Once one obtains the normalized left $[\Psi]$ and right $[\phi]$ eigenvectors of the eigenvalue problem, the spectral decomposition of the matrices can be performed. Eq. (28) can be transformed in the following by normalization using the modal matrix $[\Psi]$ and $[\phi]$:

$$[I]\{\ddot{y}_p\} + [\Lambda]\{y_p\} - \varepsilon_1\cos(\lambda_f\tau)[\bar{K}_{ft}]\{y_p\} = 0, \tag{29}$$

where $[\psi]^{\mathrm{T}}[\bar{M}][\phi] = [I]$, $[\psi]^{\mathrm{T}}[\bar{K}][\phi] = [\Lambda]$ and $\beta_{cr}[\psi]^{\mathrm{T}}[\bar{K}_f][\phi] = [\bar{K}_{ft}]$.

Eq. (29) can be rewritten as

$$\frac{\mathrm{d}^2}{\mathrm{d}\tau^2}y_p + \lambda_p^2 y_p - \varepsilon_1\cos(\lambda_f\tau)\sum_{q=1}^{M} f_{pq}y_p = 0. \tag{30}$$

Now, suppose that y_p in the following form to use the method of multiple scales:

$$y_p(\tau,\varepsilon) = y_{p0}(T_0,T_1,T_2) + \varepsilon y_{p1}(T_0,T_1,T_2) + \varepsilon^2 y_{p2}(T_0,T_1,T_2) + \cdots, \tag{31}$$

where $\varepsilon(=-\varepsilon_1/2)$ is the perturbation parameter and T_n is expressed as $\varepsilon^n\tau$. Through the first order approximation, i.e., by considering the only first two terms in Eq. (31), we can define the transition curves that separate stable solutions from unstable ones in the $\varepsilon_1 - \lambda_f$ plane. High order expansions can express the transition curves as more exact and high-order function. However, if we restrict ε_1 within a specific value, the first order expansions also produce a good result [20]. The results can be summarized as follows.

If λ_f is near $\lambda_p + \lambda_q$ and $f_{pq} f_{qp} > 0$,

$$\lambda_f = \lambda_p + \lambda_q \pm \left(\frac{\varepsilon_1}{2}\right) \Lambda_{pq} + O(\varepsilon_1^2), \quad \Lambda_{pq} = \left(\frac{f_{pq} f_{qp}}{\lambda_p \lambda_p}\right)^{1/2} \tag{32}$$

and if λ_f is near $\lambda_p - \lambda_q$, $f_{pq} f_{qp} < 0$, and $\lambda_p > \lambda_q$,

$$\lambda_f = \lambda_p - \lambda_q \pm \left(\frac{\varepsilon_1}{2}\right) \Lambda_{pq} + O(\varepsilon_1^2), \quad \Lambda_{pq} = \left(\frac{-f_{pq} f_{qp}}{\lambda_p \lambda_p}\right)^{1/2}. \tag{33}$$

From Eqs. (32) and (33), it is easily seen that the sum-type and difference-type combination resonances cannot exist simultaneously for any pair of natural frequencies λ_p and λ_q.

3. Numerical results and discussions

In this study, we used the finite element method to numerically test a simplified model of a liquid-filled structure, as shown in Fig. 1(a). And as shown in Fig. 1(b), the model of the finite element meshes is composed of the shell structure elements, the 8-node interface elements, and the interior liquid elements. And the liquid element consists of the uniform three-dimensional 20-node cubic and 15-node tetrahedron elements.

3.1. Verification

3.1.1. Comparison of natural frequencies

To check the validity of the results, we compared numerical data with those of previous work. Table 1 summarizes the material and geometric data for the cantilevered cylindrical shell model. Table 2 shows the numerical results of the present study and the theoretical and experimental results [21,22]. These data obtained by applying the clamped-free boundary condition, show good agreement between the present work and the previous results.

3.1.2. Free-surface effect

Figs. 2 and 3 show the influence of motion of the free surface of the fluid. Several cylindrical shells are considered in order to provide a sufficiently large series of results to show the effect of the free surface during the vibrations. In general, as in Fig. 2, one can see that the frequencies calculated by the method including the free surface are lower than those given by Ref. [22]. At the

Table 1
Material and geometric data for three type cylinders

	Cylinder A	Cylinder B	Cylinder C
ρ_S (kg/m^3)	7800	7750	7750
ρ_F (kg/m^3)	1000	1000	1000
t (mm)	1.5	1.16	0.65
R (mm)	77.25	99.58	99.33
L (mm)	231	398	280
H/L (%)	0, 100	80	50

Table 2
The dimensionless natural frequencies of the cylindrical shells for the filling ratio

Cyl.	H/L	(n,m)	Frequency (10^{-2})		
			Theory [21]	Present work	Experiment [21]
A	0	(1,3)	5.721	5.717	5.563
		(1,4)	8.554	8.553	8.533
		(1,5)	13.374	13.367	13.361
A	1.0	(1,3)	3.618	3.548	3.504
		(1,4)	5.718	5.710	5.671
		(2,4)	10.030	10.030	9.880
			Theory [22]	Present work	Experiment [22]
B	0.8	(1,3)	2.275	2.251	2.205
		(1,2)	2.832	2.762	2.356
		(1,4)	2.913	3.400	3.435
C	0.5	(1,4)	3.183	3.199	3.195
		(1,3)	3.693	3.693	3.635
		(1,2)	6.297	6.297	5.672

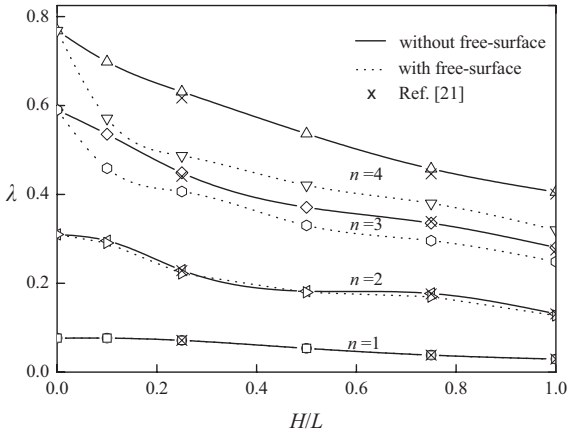

Fig. 2. Comparison of frequencies between the results (with and without free-surface effects) and those of Ref. [22] (without free-surface effects) for the clamped-free case ($m = 2, R/t = 100, L/R = 3$).

lower frequencies, the free-surface effect is approximately 1–3%, which is negligible. In contrast, this effect becomes more pronounced at higher axial modes. This phenomenon is attributed to the kinetic energy developed by the free surface in motion, which lowers the natural frequencies of the system to different levels as a function of other initial conditions: geometrical and physical characteristics, number of axial and circumferential modes.

The effect of the free surface is stronger particularly for wide shells, where one will notice a reduction of the frequencies once there is a little fluid in the shell. The greatest difference is observed at approximately $H/L \approx 0.2$, whereas for fluid levels from $H/L = 0.5$–1.0 the variations are more moderate.

In Fig. 3, one can see that the most significant deviations are to be found with the shortest shells, such as $L/R = 3$. As the ratio L/R is higher, the difference between the two cases becomes smaller. In addition, the smallest deviation between the frequencies occurs when the shell is full, $H/L = 1.0$. On the other hand, the potential energy due to the height of the waves has only a slight bearing on frequency variation as it can readily be seen that it is far smaller than the strain energy of the solid shell.

3.2. Typical modes of instability

First, we must define and examine the mode shapes which induce various types of instability. The modes of a free–free cylindrical shell can be grouped by the number of circumferential waves m. Here, the case $m = 0$ is not examined, because the modes with $m = 0$ does not induce critical load. Fig. 4 describes the schematic shapes of various modes. The mode shapes for $m = 1$ are

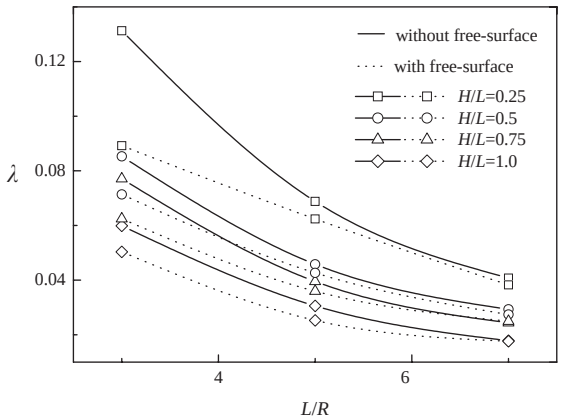

Fig. 3. Frequency variation as a function of L/R and comparison between the results with free-surface effects and without free-surface effects for clamped-free case ($m = 2, n = 3, R/t = 300$).

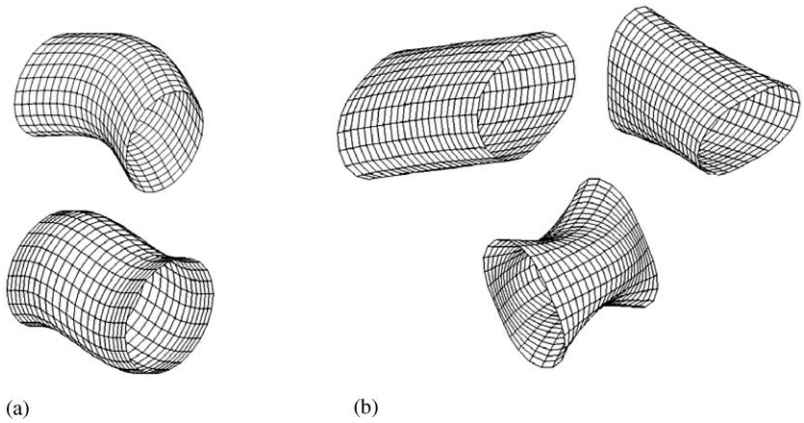

Fig. 4. Schematic shapes of various modes. (a) First bending and second bending modes ($m = 1$). (b) Constant and linear axial modes and first bending mode ($m = 2$).

beam-like modes as presented in Fig. 4(a). In this work, those modes are called first bending mode ($n = 2$), second bending mode ($n = 3$), and so forth by the number of extrema in the longitudinal direction. If the number of circumferential waves m is equal to or greater than two, the free–free cylindrical shell has two sets of modes, which have a linear or constant axial deformation ($n = 0, 1$), and the other modes demonstrate more severe bending in the longitudinal direction and are called the first bending mode ($n = 2$), second bending mode ($n = 3$), and so on, similarly to the modes of $m = 1$, as shown in Fig. 4(b).

3.3. Follower force

3.3.1. Constant follower force

The dynamic stability of liquid-filled shells under a follower force was studied for the stepwise H/L ranged 0–1, $L/R = 20$, 30, 40, 60, 80, and $t/R = 0.03$, 0.1, 0.2. Fig. 5 shows the typical

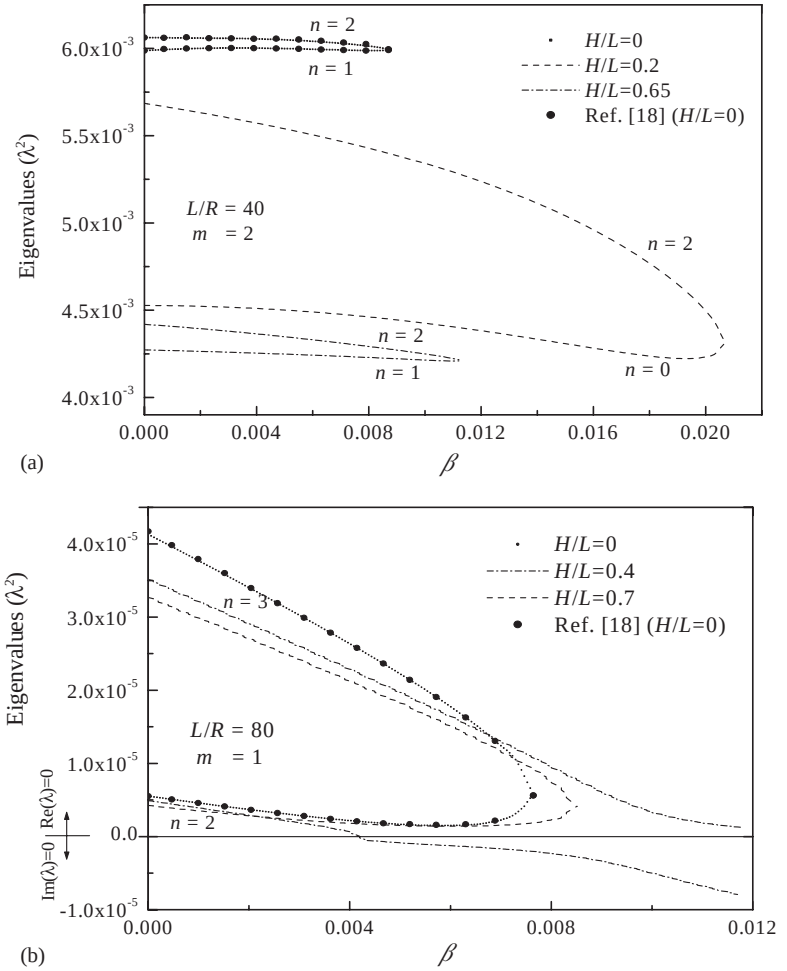

Fig. 5. Eigenvalue curves of typical instability types for filling ratio ($t/R = 0.1$).

instability types of free–free cylindrical shells under a follower force for various filling ratios. The eigenvalue curves for $H/L = 0$ which has two modes ($n = 1, 2$ for Fig. 5(a), and $n = 2, 3$ for Fig. 5(b)) including a flutter instability are compared with the data in Ref. [18], and the results appear to agree well. The instability type of cylindrical shell containing fluid changes as the filling ratio varies. In Fig. 5(a), the flutter-type instability determines the critical load for various filling ratios, and the instabilities occurs at modes $m = 2$. The critical load which has the two modes ($n = 0, 2$) is very large for low filling ratio. Similarly, the shell with $L/R = 20$ shows flutter-type instability at the same circumferential mode. The frequency of the each mode decreases as the filling ratio is increased, as shown in Refs. [21,22]. These flutter-type instabilities occur as the thickness and the length ratio are decreased, and have critical load at $m \geqslant 2$. Fig. 5(b) shows that depending on the filling ratio, both divergence and flutter instability can occur, and this change of instability type is also shown for the case of beam with a concentrated mass [23]. The instability occurs at the modes $m = 1$, and the two modes including a flutter instability are the first bending mode and the second bending mode in Fig. 4(a), which are beam-like modes [18]. Based on these data, we found that the first instability type changes from the flutter instability when $H/L \leqslant 0.08$ to the flutter and divergence instability when $0.08 < H/L < 0.23$, to divergence instability when $0.23 \leqslant H/L \leqslant 0.58$, and finally to flutter instability when $0.58 < H/L$. These divergence-type instabilities occur when the beam-like modes are dominant in the shell, such as long and thick shell.

Fig. 6 shows the critical values versus the filling ratio for various lengths of the shell. In general, the critical force for empty shells increases as the length ratio is decreased [18]. However, the critical force increases for some ranges of the lower filling ratio as the length ratio is increased. In Fig. 6(a), the critical forces of the shell for the various filling ratios are greater than the critical force of the shell when $H/L = 0$; that is, the liquid filled thin shell is more stable than the empty shell, except for the short shell when $H/L \leqslant 0.08$ in which $m = 3$ shifts to $m = 2$. As shown in Fig. 6, this lower critical force at the low filling ratios occurs for the short shell. In Figs. 6(b) and (c), the critical forces of both the long shell, which has a divergence-type instability region, and the short shell for the low filling ratios are less than the critical force of the shell when $H/L = 0$. Therefore, the shell containing fluid in those ranges is more unstable than the empty shell.

In Fig. 6(b), the critical force does not change as the filling ratio is increased in some ranges along the horizontal axis. These ranges are located near large filling ratios for the flutter-type instability, and the critical force is slightly larger than that of the empty shell in those ranges. This region increases as the length ratio and the thickness ratio are increased, as shown in Fig. 6.

The divergence-type instability, which is indicated by the region bulging downward, occurs as the length ratio and the thickness ratio are increased and appears only when $H/L \leqslant 0.6$. As shown in Figs. 6(b) and (c), the divergence region determines the instability of the shell.

For the lower filling ratio, the critical forces change rapidly and widely as the filling ratio is increased, and the decrement of the critical force decreases or vanishes as the length ratio is increased, and this phenomenon occurs in flutter-type instability. In Fig. 6(b), for the shell with $L/R = 20$, 30 and 40, the smallest critical force occurs in flutter-type instability for $H/L \leqslant 0.1$, while for the shell with $L/R = 60$ and 80, in divergence-type instability for $0.13 \leqslant H/L \leqslant 0.15$. This pattern is similar for other thickness ratios, except for the thin shell whose higher circumferential modes are dominant. The minimum critical load occur at the low filling ratio, $H/L \leqslant 0.15$, where the liquid filled shell is the most unstable. In addition, the short shell shows flutter type instability,

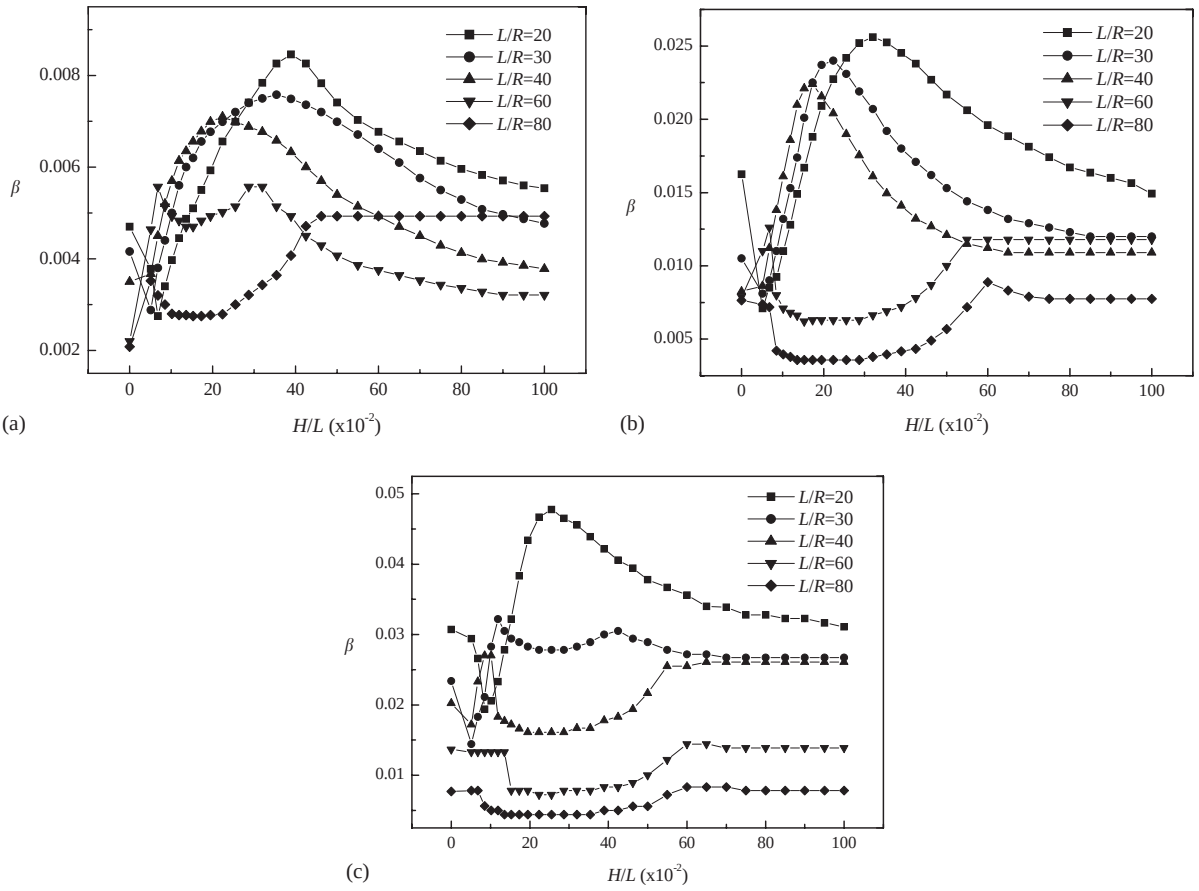

Fig. 6. (a) Critical load for various length of the shells ($t/R = 0.03$). (b) Critical load for various length of the shells ($t/R = 0.1$). (c) Critical load for various length of the shells ($t/R = 0.2$).

and the long shell the divergence type instability in that region. This rapid change in the low filling ratio and the existence of the steady critical force in the large filling ratio mean that the fluid is influenced more by the follower force as the fluid is near the bottom where the follower force acts.

3.3.2. *Pulsating follower force*

The instability region in $\varepsilon_1 - \lambda_f$ plane for each combination of eigenvalues λ_p and λ_q can be determined by the vertex $\lambda_p \pm \lambda_q$ and the bandwidth parameter Λ_{pq} for the first order expansion as given by Eqs. (32) and (33), where the bandwidth parameter Λ_{pq} is an important factor for determining the width of unstable regions. Therefore, we focus on the bandwidth parameter in the present study.

In Figs. 7 and 8, the relation between the bandwidth parameter Λ_{pq} and the constant load parameter ε_0 is shown for various filling ratios. The type of combination resonance and the transition are also presented. For Figs. 7 and 8, the analyzed circumferential wave number is that

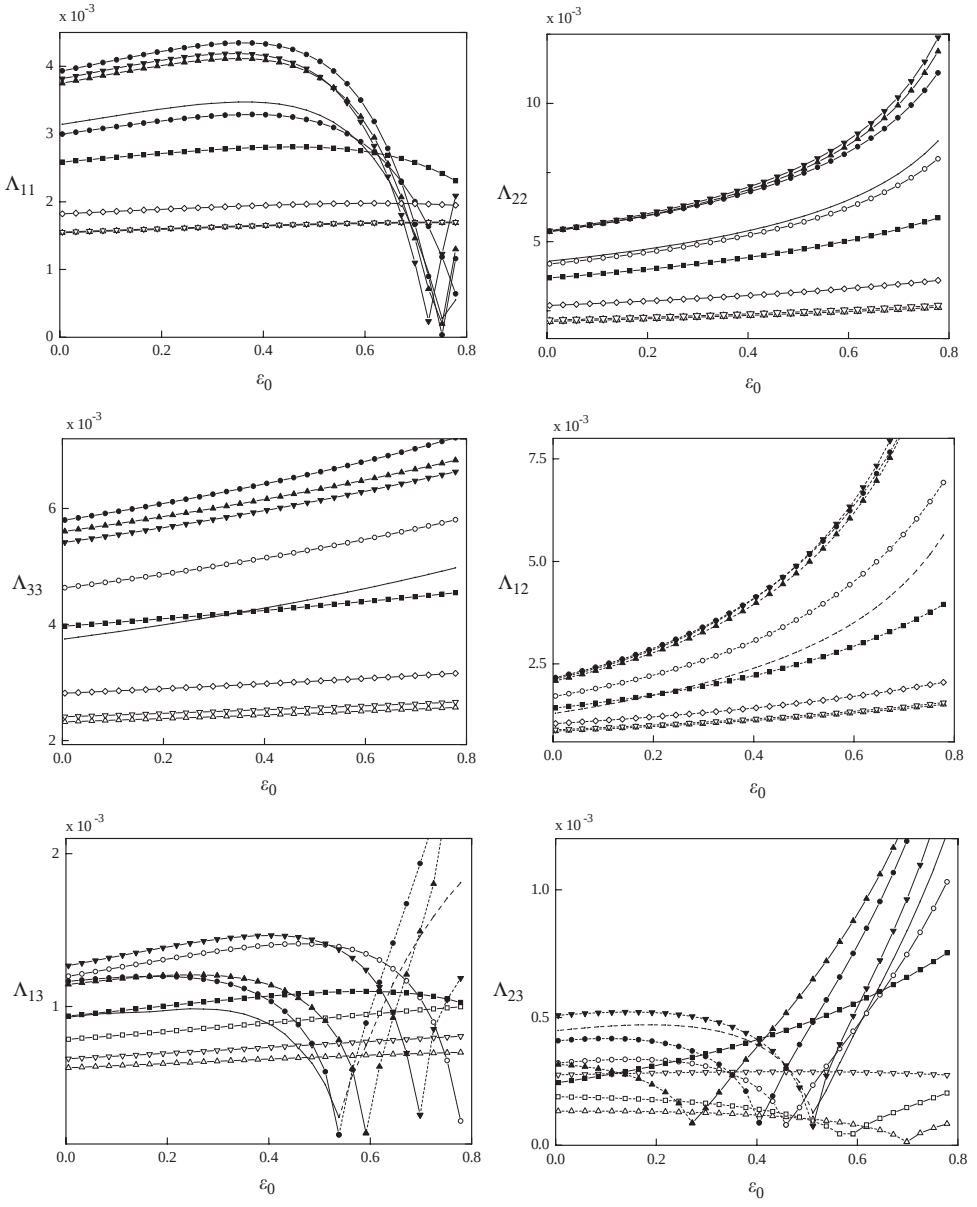

Fig. 7. Bandwidth parameter versus constant load parameter for various filling ratios ($m = 1, t/R = 0.1, L/R = 80$) [——, 0; —△—, 0.15; —▽—, 0.25; —□—, 0.4; —▩—, 0.5; —▼—, 0.65; —▲—, 0.8; —●—, 1.0].

inducing the critical load for the constant load case. In these figures, the solid line indicates the sum type resonance and the dash line represents the difference type resonance. The difference type resonance means that the resonance takes place in low driving frequencies, and this phenomenon is significant in the stability sense.

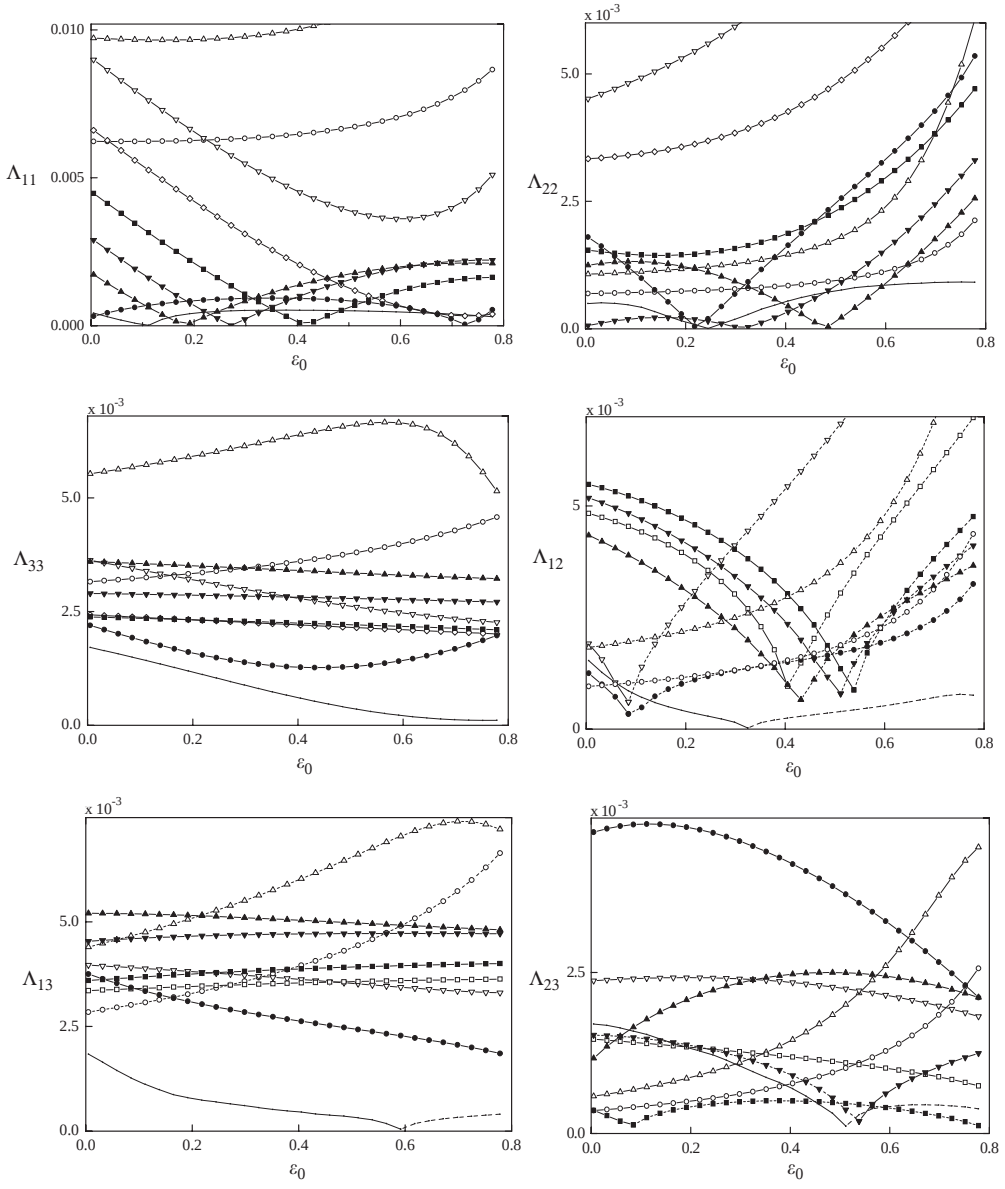

Fig. 8. Bandwidth parameter versus constant load parameter for various filling ratios ($m = 2, t/R = 0.03, L/R = 20$) [——, 0; —○—, 0.1; —△—, 0.2; —▽—, 0.4; —□—, 0.5; —▩—, 0.6; —▼—, 0.7; —▲—, 0.8; —●—, 1.0].

For the case of the long shell which has $m = 1$ and beam-type modes dominantly where the subscript 1, 2 and 3 indicate first, second and third bending modes, respectively, the transition of type occurs for only two combination, $\lambda_1 \pm \lambda_3$ and $\lambda_2 \pm \lambda_3$. At the point where the transition takes place, the bandwidth parameter is 0. For the combination resonance near $\lambda_1 \pm \lambda_3$ the transition of type occurs for only high filling ratio ($H/L > 0.5$) and the transition point decreases as the filling ratio is increased. The bandwidth parameters of resonances near $2\lambda_2$, $2\lambda_3$ and $\lambda_1 - \lambda_2$ show

similar tendencies. However, $\lambda_1 \pm \lambda_2$ has different type resonance for all filling ratios. This means that this combination resonance plays a more important role in terms of stability. For the three resonance regions, the bandwidth parameter increases monotonically. The bandwidth parameter of resonance near $2\lambda_1$ for high filling ratio becomes zero around $\varepsilon_0 \approx 0.75$. Note that the eigenvalue curve for the first bending mode in Fig. 5(b) also has a minimum eigenvalue near $\varepsilon_0 \approx 0.75$ as discussed in Ref. [20] for a beam model. Note also that λ_{22} and λ_{12} are relatively larger than other resonances. As for the effect of the filling ratio on the long shell, note that for low filling ratio Λ_{pq} is smaller than that of zero filling ratio, and then, is seen that Λ_{pq} increases as the filling ratio is increased for the resonances near all combinations of eigenvalues.

The bandwidth parameters for the short shell which has $m = 2$ are shown in Fig. 8, where the subscripts 1, 2 and 3 indicate the constant, linear axial modes and first bending modes, respectively, as shown in Fig. 4(b). For this case, the transition of type occurs for only two combination, $\lambda_1 \pm \lambda_2$ and $\lambda_2 \pm \lambda_3$ for some filling ratios. For the resonance near $\lambda_1 \pm \lambda_2$, the transition points for low filling ratios ($0.3 < H/L < 0.6$) increases as the filling ratio is increased while those for high filling ratio ($0.6 < H/L$) decreases as the filling ratio is increased. The curves for $\lambda_2 \pm \lambda_3$ for high filling ratio can be seen to shift to the left with increasing value as the filling ratio is increased. For the low filling ratio, Λ_{pq} increases to that of $H/L < 0.3$ and then decreases. For the direct parametric resonances near $2\lambda_1$, $2\lambda_2$, the bandwidth parameter has zero value at specific values of ε_0, which coincides approximately with the constant load β_0 at which the eigenvalue curves of the modes shows a maximum in Fig. 5(a).

Figs. 9 and 10 show the dynamic instability regions for various filling ratios at $\varepsilon_0 = 0.1$ and show low driving frequency regions which is significant in terms of stability. For the long shell in Fig. 9, the instability regions observed near $2\lambda_1$ and $\lambda_2 - \lambda_1$ for low filling ratio are smaller than those for high filling ratio. The driving frequency of $2\lambda_1$ and $\lambda_2 - \lambda_1$ decreases as the filling ratio is increased.

For the short shell in Fig. 10, the difference type resonances of $\lambda_2 - \lambda_1$, $\lambda_3 - \lambda_1$ appear for $H/L < 0.4$ where the frequencies of this type of resonances increase as the filling ratio is increased

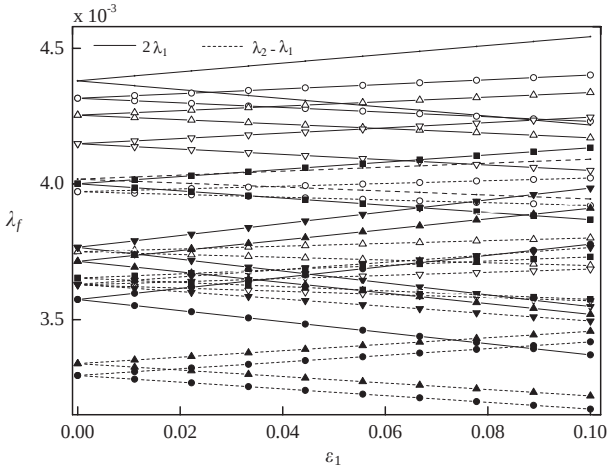

Fig. 9. Parametric instability region for various filling ratios ($m = 1, t/R = 0.1, L/R = 80$) [$H/L$ values respectively: ——, 0; —○—, 0.1; —△—, 0.25; —▽—, 0.35; —▩—, 0.5; —▼—, 0.65; —▲—, 0.85; —●—, 1.0].

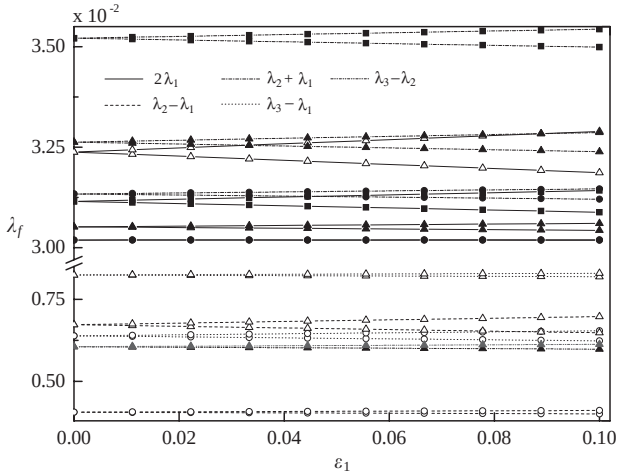

Fig. 10. Parametric instability region for various filling ratios ($m = 2, t/R = 0.03, L/R = 20$) [$H/L$ values respectively: —○—, 0.1; —△—, 0.3; —▩—, 0.5; —▲—, 0.7; —●—, 0.9].

while the frequencies for $H/L > 0.4$ decrease as the filling ratio is increased. The instability region for $H/L > 0.4$ is also seen to decrease as the filling ratio is increased. $\lambda_2 \pm \lambda_3$ for $0.5 < H/L < 0.8$ appears in low driving frequency due to the different type resonance that occur in those filling ratios as shown in Fig. 8.

4. Conclusions

A partially liquid-filled cylindrical shell subjected to a thrust is investigated using a finite element method, and the thrust is modelled as a constant follower force and a pulsating follower force. Results of the analysis of the present study can be summarized as followers.

First, in the case of the constant follower force:

1. For various filling ratios, the flutter-type instability of the system, which occurs in $m \geqslant 2$, changes to the divergence type instability, and the divergence-type instability region that occurred in $m = 1$ increases as the length ratio and the thickness ratio are increased. But the divergence region is observed to occur only in the region $H/L \leqslant 0.6$.
2. For the lower filling ratios, the critical forces change rapidly and widely as the filling ratio is increased, and the decrement of critical force decreases or vanishes as the length ratio is increased; this latter phenomenon occurs in flutter-type instability. The minimum critical load that occurs in the low filling ratio, $H/L \leqslant 0.15$, at which the liquid filled shell is the most unstable.
3. For the higher filling ratio, in some regions, the critical force does not change with the increase of the filling ratio as the length ratio and the thickness ratio are increased.
4. The fluid is more influenced by the follower force as the fluid is near to the bottom where the follower force acts.

Second, in the case of pulsating follower force:

1. For the long shell ($m = 1$), Λ_{pq} has large value for $H/L > 0.5$ where the instability regions are larger than those for the low filling ratios. The driving frequencies decrease as the filling ratio is increased. For large filling ratio, the system is more unstable than the system without fluid due to pulsating load.
2. For short shell ($m = 2$), Λ_{pp} has large value for the low filling ratio and the combination resonance has different type resonance for low filling ratio. The driving frequencies decrease for high filling ratio with decreasing the instability region while the frequencies increase for low filling ratio.
3. The filling ratio has a large effect on the system subjected to a pulsating follower force, especially on the system $m \geqslant 2$.

For further study on liquid propelled launcher, we plan to include the payload and feedline system, which is accompanied by fluctuations in the liquid pressures, especially at the fuel feed inlets in the propulsion unit.

Acknowledgements

This work was supported by Korea Research Foundation Grant (KRF-2002-041-D00102).

Appendix A. Nomenclature

R_F, R_S	domain of fluid and structure at equilibrium
R_I	fluid–structure contact surface
R_{FS}	free-surface at equilibrium
P	pressure field in the liquid
φ	displacement potential field in the liquid
u_i	displacement field in the structure
n	unit normal (external to the fluid boundary)
B	bulk modulus
ρ_F, ρ_S	mass density of fluid and structure
τ_{ij}	cauchy stress tensor
ε_{ij}	deformation tensor of elastic media
υ	Poisson ratio
E	Young's modulus
ω	natural frequency of the shell
λ	non-dimensionalized natural frequency
λ_f	non-dimensionalized driving frequency
τ	non-dimensionalized time
ε_0	constant load parameter
ε_1	pulsating load parameter
Λ_{pq}	bandwidth parameter

g	gravity
F	constant follower force
$\beta(t)$	non-dimensionalized follower force
β_0	non-dimensionalized constant part of a follower force
β_1	non-dimensionalized pulsating part of a follower force
β_{cr}	non-dimensionalized critical load
y_p	orthogonalized co-ordinate
m, n	circumferential and axial mode
L, R, t	length, mean radius, thickness of a shell
H	fluid height
π	fluid–structure interaction functional
x, y, z	local co-ordinate of mean surface of the shell
u, v, w	displacement of the mean surface of the shell according to the direction x, y, z
Ψ, Φ	normalized left and right modal matrices
K_F	stiffness matrix of the shell due to follower force
$\tilde{M}, \tilde{K}$	mass and stiffness matrix considering compressible fluid
M^*, K^*	mass and stiffness matrix considering incompressible fluid with free-surface
$\bar{M}, \bar{K}, \bar{K}_f$	non-dimensionalized mass, stiffness and geometric stiffness matrices

References

[1] H.J.P. Morand, R. Ohayon, *Fluid Structure Interaction, Applied Numerical Methods*, Wiley, Singapore, 1995.
[2] G.W. Housner, The dynamic behavior of water tanks, *Bulletin of the Seismological Society of America* 53 (1963) 381–387.
[3] A.S. Veletsos, J.Y. Yang, Dynamic of fixed-based liquid-storage tanks, *Proceedings of US–Japan Seminar Earthquake Engineering, Research*, 1976, pp. 317–341.
[4] R. Ohayon, H. Morand, Substructure variational analysis of the vibrations of coupled fluid-structure systems, *International Journal for Numerical Methods in Engineering* 14 (1979) 741–755.
[5] R. Ohayon, H. Morand, Mechanical and numerical modelling of fluid-structure vibration instabilities of liquid propelled launch vehicle, *Chaos, Solution & Fractals* 9 (1995) 1705–1724.
[6] Mohammad Aslam, Finite element analysis of earthquake-induced sloshing in axisymmetric tanks, *International Journal for Numerical Methods in Engineering* 17 (1981) 159–170.
[7] G. Sandberg, P. Goransson, A symmetric finite element formulation for acoustic fluid-structure interaction analysis, *Journal of Sound and Vibration* 123 (1988) 507–515.
[8] W.C. Muller, Simplified analysis of linear fluid-structure interaction, *International Journal for Numerical Methods in Engineering* 17 (1981) 113–121.
[9] M.A. Hamdi, Y. Ousset, A displacement method for the analysis of vibrations of coupled fluid-structure systems, *International Journal for Numerical Methods in Engineering* 13 (1978) 139–150.
[10] L.G. Olson, K.J. Bathe, A study of displacement-based fluid finite elements for calculating frequencies of fluid and fluid-structure systems, *Nuclear Engineering and Design* 76 (1983) 137–151.
[11] E.L. Wilson, E. Khalvati, Finite elements for the dynamic analysis of fluid-solid systems, *International Journal for Numerical Methods in Engineering* 19 (1983) 1657–1983.
[12] Y.S. Kim, C.B. Yun, A spurious free four-node displacement-based fluid element for fluid-structure interaction, *Engineering Structures* 19 (1997) 665–678.
[13] W.J.T. Daniel, Modal methods in finite element fluid-structure eigenvalue problems, *International Journal for Numerical Methods in Engineering* 15 (1980) 1161–1175.

[14] V.V. Bolotin, *Non-conservative Problems of the Theory of Elastic Stability*, Pergamon Press, Oxford, 1963.
[15] Y.H. Kim, S.W. Lee, A solid element formulation for large deflection analysis of composite shell structures, *Computers & Structures* 30 (1988) 269–274.
[16] C. Cho, H.C. Park, S.W. Lee, Stability analysis using a geometrically nonlinear assumed strain solid shell element model, *Finite Elements in Analysis and Design* 29 (1998) 121–135.
[17] Meirovitch, *Analytical Methods in Vibrations*, Macmillan, New York, 1967.
[18] S.-H. Park, J.-H. Kim, Dynamic stability of a completely free circular cylindrical shell subjected to a follower force, *Journal of Sound and Vibration* 231 (2000) 989–1005.
[19] A.H. Nayfeh, D.T. Mook, Parametric excitation of linear systems having many degrees of freedom, *Journal of the Acoustical Society of America* 62 (1977) 375–381.
[20] Y.S. Choo, J.-H. Kim, Dynamic stability of a free–free Timoshenko beam subjected to a pulsating follower force, *Journal of Sound and Vibration* 216 (1998) 623–636.
[21] T. Mazuch, J. Horacek, J. Trnka, J. Vesely, Natural modes and frequencies of a thin clamped-free steel cylindrical storage tank partially filled with water: FEM and measurement, *Journal of Sound and Vibration* 193 (1996) 669–690.
[22] J. Mistry, J.C. Menezes, Vibration of cylinders partially filled with liquid, *Journal of Vibration and Acoustics* 117 (1995) 87–93.
[23] Y.P. Park, C.D. Mote, The maximum controlled follower force on a free–free beam carrying a concentrated, *Journal of Sound and Vibration* 98 (1985) 247–256.